



HAL
open science

Thermal behavior of Mg–Ni-phyllsilicate nanoscrolls and performance of the resulting composites in hexene-1 and acetone hydrogenation

Ekaterina K Khrapova, Valery L Ugolkov, Elena A Straumal, Sergey A Lermontov, Vasily Lebedev, Daniil A Kozlov, Tatyana S Kunkel, Alexandre Nominé, Stephanie Bruyere, Jaafar Ghanbaja, et al.

► To cite this version:

Ekaterina K Khrapova, Valery L Ugolkov, Elena A Straumal, Sergey A Lermontov, Vasily Lebedev, et al. Thermal behavior of Mg–Ni-phyllsilicate nanoscrolls and performance of the resulting composites in hexene-1 and acetone hydrogenation. *ChemNanoMat*, 2021, 7 (3), pp.257-269. 10.1002/cnma.202000573 . hal-03349882

HAL Id: hal-03349882

<https://hal.science/hal-03349882>

Submitted on 14 Oct 2021

HAL is a multi-disciplinary open access archive for the deposit and dissemination of scientific research documents, whether they are published or not. The documents may come from teaching and research institutions in France or abroad, or from public or private research centers.

L'archive ouverte pluridisciplinaire **HAL**, est destinée au dépôt et à la diffusion de documents scientifiques de niveau recherche, publiés ou non, émanant des établissements d'enseignement et de recherche français ou étrangers, des laboratoires publics ou privés.

Thermal behavior of Mg–Ni-phyllsilicate nanoscrolls and performance of the resulting composites in hexene-1 and acetone hydrogenation

Ekaterina K. Khrapova^a, Valery L. Ugolkov^b, Elena A. Straumal^c, Sergey A. Lermontov^c, Vasily A. Lebedev^d, Daniil A. Kozlov^e, Tatyana S. Kunkel^{a,f}, Alexandre Nominé^g, Stephanie Bruyere^h, Jaafar Ghanbaja^h, Thierry Belmonte^h, Andrei A. Krasilin^{a,*}

^aToffe Institute, 26 Politekhnikeskaya st., St. Petersburg 194021, Russia

^bGrebenshchikov Institute of Silicate Chemistry of the RAS, 2 Makarova emb., St. Petersburg 199034, Russia

^cIPAC RAS, Severny 1, Chernogolovka 142432, Russia

^dBernal Institute, University of Limerick, Limerick V94 T9PX, Ireland

^eFaculty of materials science, Lomonosov Moscow State University, 1-73 Leninskiye Gory, Laboratory Building B, 119991 Moscow, Russia

^fMoscow Institute of Physics and Technology, 9 Institutskiy per., Dolgoprudny 141701, Russia

^gDepartment of Physics and Engineering, ITMO University, 49 Kronverksky pr., St. Petersburg 197101, Russia

^hInstitut Jean Lamour, Université de Lorraine, UMR CNRS 7198, Nancy F-54011, France

KEYWORDS nanotubes, hydrothermal synthesis, reduction, metal, nanoparticles, heterogeneous catalysis

ABSTRACT: Here we report on the thermal properties of Mg–Ni-phyllsilicate nanoscrolls as a promising precursor for production of Ni/silicate composite catalysts. Spontaneous scrolling of the phyllsilicate layer originating from size difference between metal-oxygen and silica sheets provides an increased surface area of future catalyst support. Metal nanoparticles can be obtained directly from the matrix by H₂ reduction. Despite the system has already been used for methane reforming, little attention has been paid to the control of size distribution of Ni nanoparticles, as well as to the reduction process itself. In order to close the gap, we carried out a thermal study of (Mg_{1-x}Ni_x)₃Si₂O₅(OH)₄ nanoscrolls in air and in H₂ environments. The phyllsilicate structure passed through a number of transformations including partial dehydroxylation with formation of sepiolite-like phase followed by silicate or oxide crystallization. Temperature ranges of these transitions overlapped with the reduction process sophisticating the H₂ consumption profiles. In particular, some amount of Ni²⁺ got sealed up by the sepiolite structural features, that opened a path for the tuning of Ni⁰:Ni²⁺ ratio of the catalyst. An increase of Ni content in the system yielded a decrease in the metal nanoparticles sizes due to both high intensity of nucleation and type of residual matrix (mostly amorphous or crystalline). In turn, size distribution and specific surface area of the composite catalysts governed conversion rate of hexene-1 and acetone hydrogenation.

INTRODUCTION

A number of layered hydrosilicate particles can gain spontaneous curvature due to an excess of strain energy and difference in chemical composition on the opposite sides of the layer.^{1–4} In 1:1 phyllsilicate like chrysotile and halloysite, strain originates from size difference between covalently bounded metal oxide and silicon oxide sheets. In addition, surface of metal (magnesium, aluminum) oxide sheet is highly hydroxylated causing large surface energy difference between the two surfaces.^{5–7} As a result, those hydrosilicates form multi-walled nanotubes and nanoscrolls, that could be found in nature^{4,8,9} or synthesized by a hydrothermal process.^{10–14} Synthesis allows the tuning of chemical composition of phyllsilicates by doping them with Fe,^{15–17} Co,^{18,19} Ni,^{1,20–27} Ti,^{28,29} Ge,^{30–32} and other cations, which yields change in properties^{24,33,34} and morphology up to stabilization of platy particles.^{16,31,32}

High specific surface area becomes one of the results of the scrolling process making the nanoscrolls suitable for adsorp-

tion^{35–39} and catalytic applications.⁴⁰ Lafay et al.⁴¹ reported on 250 m²/g for chrysotile nanoscrolls, and Belkassa et al.⁴² demonstrated an increase of the specific surface area from 61 to 503 m²/g by chemical etching. High values up to 315 m²/g were achieved for Ni phyllsilicates.^{43,44} In comparison with 3D zeolites and other porous materials, nanotubes and nanoscrolls have quasi-1D channel pore, that gives rise to controllable release of its contents (for example, drugs and corrosion inhibitors) by sealing up the nanoscroll's inner channel.^{45,46} Abundance of OH-groups on the nanoscrolls surface facilitates its further chemical modification by organic molecules or inorganic nanoparticles boosting up adsorption,^{47–49} sensing,⁵⁰ and catalytic performance.^{51–58}

An intriguing feature of *d*-element based nanoscrolls is the metal nanoparticles formation during H₂ heat treatment. In addition to relatively high specific surface area of initial phyllsilicate, these particles are tightly bounded with the support. Ni, Cu, and Co-based phyllsilicate materials demonstrated good catalytic activity in dry reforming of methane,^{43,59–61}

Fischer-Tropsch process,¹⁹ and hydrogenation process.^{62,63} In perspective, initial nanoscrolls could be designed on the basis of multiple *d*-element cations, thus supporting advantages of bimetallic catalysis.^{61,64,65}

Hydrogen treatment results in metal nanoparticles formation, but the heat action itself causes the phyllosilicate layer structural transformation. Thermal studies carried out on natural⁸ and synthetic^{15,22,66,67} phyllosilicate nanoscrolls reported on two principle effects: intense endothermic dehydroxylation at around 630 °C and exothermic forsterite crystallization around 820 °C. First effect was often interpreted as structure collapse, however, nanotubular morphology can still be preserved³⁸ until silicate crystallization.

The aim of this work was to study peculiarities of Ni reduction in Mg-Ni-phyllosilicate nanoscrolls in the view of their catalytical application, in particular, to distinguish between the effect of temperature increase and H₂ chemical action on the nanoscrolls structure and morphology.

EXPERIMENTAL SECTION

Nanoscrolls synthesis

Phyllosilicate (Mg_{1-x}Ni_x)₃Si₂O₅(OH)₄ nanoscrolls with nominal *x* = 0, 0.33, 0.5, 0.67, and 1 were synthesized by hydrothermal treatment of initial composition. The latter was prepared as follows. About of 4 g of amorphous SiO₂ (Aerosil A-300) were mixed with 100 ml of 2 M NaOH water solution. The suspension was stirred by magnetic stirrer for 24 h at room temperature until SiO₂ dissolution. Then 500 ml of 1 M (1-*x*)MgCl₂ and *x*NiCl₂ water solution was added dropwise at constant stirring. The precipitate was washed with distilled water from NaCl byproduct and excess of NaOH by decantation and vacuum filtration, dried at 90 °C in air, and grinded in an agate mortar. About of 2.0 g of initial composition was put in 400 ml stainless steel autoclave with titanium liner. The autoclave's volume was filled by 160 ml of 0.1 M NaOH water solution. The vessel was sealed, and heat treated at 350-353 °C and 21-24 MPa (the pressure was measured by U-type and digital pressure gauges) for 10 h. After cooling, the product was washed from NaOH by decantation and dried at 90 °C in air.

Heat treatment techniques

Thermal properties of the nanoscrolls obtained were investigated by synchronous thermal analysis and temperature-programmed reduction (TPR). Netzsch STA 429 CD was used as thermal analyzer working in differential scanning calorimetry and thermogravimetry regime (DSC-TG). The device was equipped with quadrupole mass spectrometer Netzsch QMS 403 C for detection of thermal decomposition products. A tablet containing about 20 mg of sample was produced by hydraulic press (the pressure was 1 kg/mm²). Tablets were analyzed in open corundum crucible in the 40-1100 °C temperature range with 20 °/min heating speed. Compressed air or 5 vol.% H₂-Ar mixture (99.995% purity) were used as a dynamic (50 ml/min) atmosphere.

TPR experiments were carried out on Chemosorb ("Nesosib", Novosibirsk). About of 0.1 g of the sample was pressed into tablet and put into gas flow reactor. The reactor was fed with 60 ml/min 10 vol.% H₂-Ar mixture (of 99.995% and 99.998% purity, respectively). Hydrogen consumption profiles were recorded in the 25-900 °C range at 20 °/min heating rate.

Catalysis of hydrogenation reactions

The nanoscrolls samples with maximal nominal Ni load (*x* = 0.67, 1) were put into the quartz gas flow reactor (a tube of 6 mm inner diameter) and exposed to 99.995 % H₂ 50 ml/min flow for 1 hour at a number of given temperatures. The exposure temperatures were chosen in the 400-900 °C range on the basis of thermal analysis. The furnace has been heated in advance up to the chosen temperature. Catalytical tests were carried out right after exposure in the same set up. Hydrogen was bubbled through one of the initial reagents, then the gaseous mixture was passed through the sample at 120 and 240 °C. Initial reagents were preheated in the case of their low volatility. Since the reaction occurred at a gas/solid interface, compliance of constant contact time between the gaseous mixture and the solid was considered to be of first priority. For that purpose, the solid sample apparent volume that had been put in the reactor was kept constant at 0.45 cm³. Three hydrogenation reactions were studied: hexene-1 to hexane conversion, acetone to isopropanol conversion, and the transformation of benzene into cyclohexane. The reaction product was cooled (in ice bath) and collected for *ex situ* nuclear magnetic resonance (¹H NMR) analysis.

Ex situ characterization

Hydrothermal and heat treatment products were characterized by powder X-ray diffraction (RXP, Rigaku SmartLab 3 operating in the Bragg-Brentano geometry, 1.5406 Å CuK_α radiation, K_β filtered, D/TEX ULTRA 250 detector working in 1D mode) in the 5-80° 2θ range with a 0.01° step. The Crystallography Open Database^{68,69} (COD) was used for the phase analysis. The PXRD peak files (for visualization purposes) were simulated by the VESTA⁷⁰ powder diffraction utility. Size distributions of Ni nanoparticles were calculated involving the most intense (111) reflection of metallic nickel by Rigaku SmartLab Studio II software. Fundamental Parameter method⁷¹ was used for the peak's convolution assuming lognormal distribution of nanoparticles size. The (Mg_{1-x}Ni_x)₃Si₂O₅(OH)₄ nanoscrolls lattice constants were refined by the Whole Powder Pattern Decomposition⁷² assuming ellipsoidal shape of crystallite.

FEI Quanta 200 scanning electron microscope equipped with EDAX energy dispersive X-ray spectrometer (SEM/EDS) was used for element content evaluation. Average sizes and morphology of the nanoscrolls and Ni particles were studied by Zeiss Libra 200 transmission electron microscope (TEM) in the bright field mode. About 200 nanoscrolls for each *x* value were used to estimate their mean length, outer and inner diameters on the basis of volumetric distribution. The volume of every nanoscroll was calculated in the hollow cylindrical approximation. Then, a weighted average value was calculated for each parameter. Ni nanoparticles size distributions based on TEM micrographs analysis accounted for at least 500 particles for each sample. Simple numerical weighted average was used to calculate the particles mean diameter.

JEOL – ARM 200 F Cold FEG was used for high-resolution microstructure characterization and element mapping (JEOL Centurio Silicon Drift Detector). The microscope was operated at 200 kV in TEM and scanning TEM (STEM) bright field and high-angle annular dark field (HAADF) modes. Gwyddion open-source software⁷³ was used for fast Fourier transform (FFT) of TEM micrographs.

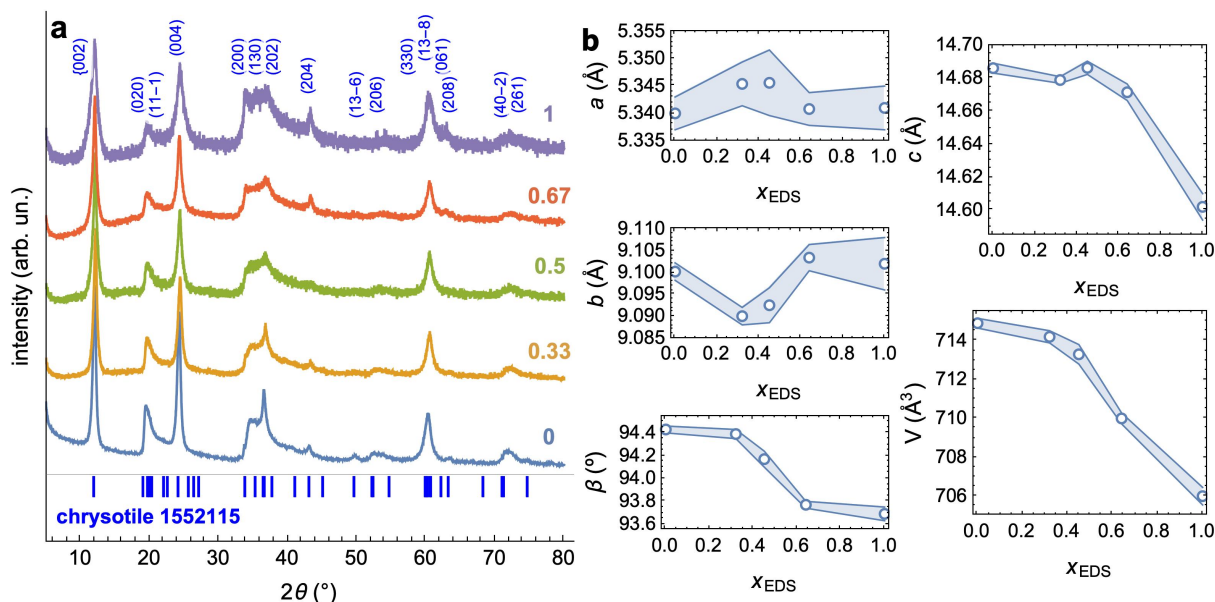


Figure 1. (a) PXRD patterns and (b) change in lattice constants of $(\text{Mg}_{1-x}\text{Ni}_x)_3\text{Si}_2\text{O}_5(\text{OH})_4$ nanoscrolls vs Ni content measured by EDS.

Table 1. Nanoscrolls chemical composition according to SEM/EDS measurements.

nominal x	Ni content by EDS, x_{EDS}	normalized element concentration, at. %				Approximate chemical formula
		Mg	Ni	Si	O	
0	0	23±4	0	15±3	62±7	$\text{Mg}_{2.98}\text{Si}_2\text{O}_5(\text{OH})_4$
0.33	0.32±0.03	15.6±0.2	7.4±0.1	16.2±0.3	60.8±0.5	$\text{Mg}_{1.93}\text{Ni}_{0.92}\text{Si}_2\text{O}_5(\text{OH})_4$
0.5	0.45±0.05	11.5±0.7	9±2	16.5±0.5	63±3	$\text{Mg}_{1.40}\text{Ni}_{1.33}\text{Si}_2\text{O}_5(\text{OH})_4$
0.67	0.64±0.05	8.5±0.2	15.1±0.2	15.9±0.2	60.5±0.3	$\text{Mg}_{1.06}\text{Ni}_{1.90}\text{Si}_2\text{O}_5(\text{OH})_4$
1	1	0	23±3	16±2	60±5	$\text{Ni}_{2.97}\text{Si}_2\text{O}_5(\text{OH})_4$

Change in the specific surface area of the samples exposed to hydrogen was studied by N_2 adsorption and desorption in the 0.01-0.99 P/P_0 range using Micromeritics ASAP 2020. Prior measurements, samples were vacuum heated at 110 °C until constant mass. Specific surface area was evaluated within the Brunauer–Emmett–Teller (BET) theory approximation.

Product content (W , at.%) after each type hydrogenation reaction was estimated by normalizing the ^1H NMR spectra integral peak intensity of product on sum of product and initial substance peak intensities. Spectra were acquired by liquid phase ^1H NMR (Bruker DPX-200, 200 MHz working frequency). Tetramethylsilane was used as an external standard.

RESULTS AND DISCUSSION

Nanoscrolls structure and morphology

Figure 1.a shows PXRD patterns of hydrothermal treatment products. All patterns were well described by the synthetic chrysotile (COD ID 1552115) obtained by Foresti et al.¹⁰ Mg^{2+} to Ni^{2+} cations substitution yielded minor crystal structure change due to the fact that these cations have close values of ionic radii: 72 pm and 69 pm,⁷⁴ respectively. That substitution

led to gradual decrease in the lattice volume. (Figure 1.b) Table 1 represents chemical composition of nanoscroll samples measured by SEM/EDS. The nickel content, measured by EDS (x_{EDS}), corresponded to its nominal content within the error.

Figure 2.a-c shows TEM micrographs of nanoscrolls as well as change in mean values of size parameters as functions of nominal x . In all cases hydrothermal process yielded different nanoscrolls fractions starting from particles with aspect ratio close to 1 up to highly anisotropic nanofibers. In this case the all dependencies of size parameters upon nominal Ni content demonstrated a maximum at $x = 0.5$. This maximum could be related to chemical composition features revealed in previous works,^{27,75,76} such as growth of conical nanoscrolls and redistribution of Mg and Ni cations along the nanoscroll's spiral. This feature can be possible because of the nanotubular phyllosilicate crystal growth, in addition to conventional crystal growth processes, is guided by a strain energy.^{1,2,77} The latter is a function of size difference between octahedral and tetrahedral sheets, in other words, a function of ionic radii of cations which constitute the layer.

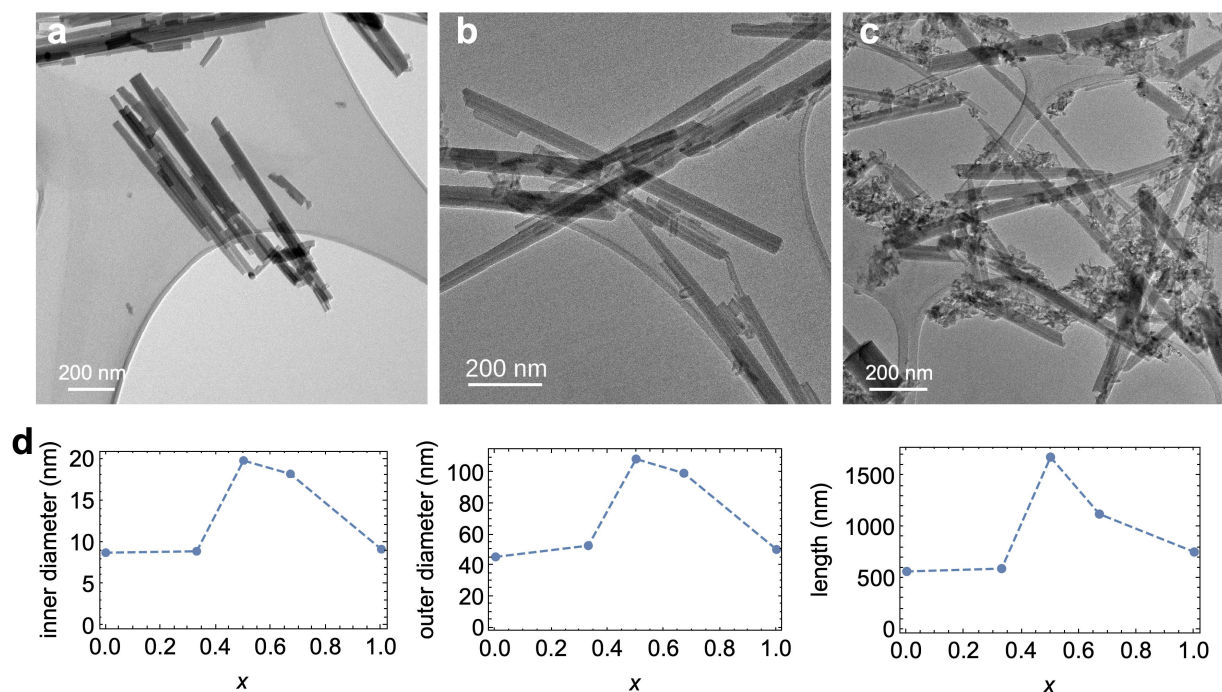


Figure 2. TEM micrographs of nanoscrolls with nominal Ni content $x =$ (a) 0, (b) 0.5, and (c) 1. (d) Weighted mean values of nanoscrolls size parameters based on their mass contribution vs nominal Ni content x .

Considering the case shown in Figure 2.d, the redistribution could increase size parameters by dividing the nanoscroll's cross section in Mg-rich core and Ni-rich shell. Relatively small Ni cations prefer forming layers of small curvature. Mg-rich nanoscrolls acted like a seed, facilitating the growth of outer Ni-rich layers. This combination, in comparison with homogeneous distribution of the cations, could result in negligible impact on the strain energy.

Thermal behavior features

Heat treatment in air

Figure 3 shows DSC-TG curves obtained in air and in H_2 -Ar atmosphere, and PXRD patterns of samples after the thermal analysis. Temperature increase in air (Figure 3.a,c) was accompanied by three principle heat effects in the ranges of 100-400 °C, 400-800 °C, and 800-1100 °C. Below 200 °C there is a small endothermal effect related to adsorbed water removal up to 4% of initial mass. The interval of 200-400 °C was characterized by small continuous mass loss without pronounced heat effects, that could be related to both removal of strongly coupled water and dehydroxylation of nanoscroll outer layers.

The 400-800 °C range contained intense but broad endo-effect with mass loss up to 9% in air. This effect could be caused by volume dehydroxylation²² together with structural transformation of sample into sepiolite-like $Mg_4Si_6O_{15}(OH)_2$ phase shown by Krasilin et al.³⁸ Because sepiolite differs from $Mg_3Si_2O_5(OH)_4$ chrysotile by Mg:Si ratio, this transformation could also be accompanied with partial amorphization. Increase in Ni content split the peak (see inset on Figure 3.a) into at least two parts. Temperature of the shoulder was ap-

proximately equal to that of the sample with $x = 1$, while the main peak's temperature shifted from 635 °C ($x = 0$) to 649 °C ($x = 0.33$) and 637 °C ($x = 0.5$). We attributed this splitting to the effect of cations redistribution along the nanoscroll's spiral as mentioned elsewhere.²⁷ The Ni-rich shell of the nanoscroll could dehydroxylate at lower temperature (585-587 °C) thus serving as a sacrificial layer against heat action. If, on the contrary, Mg and Ni cations were distributed nonuniformly between the particles but homogeneously in the scrolled layer of every particle, then one should expect gradual decrease in the peak temperature without occurrence of the shoulder peak. As far as the sepiolite-like phase still contained some number of OH-groups, it dehydroxylated continuously in the 640-800 °C range, which could be confirmed by the mass loss curves. (Figure 3.c)

Strong and narrow exo-effect in the 800-1100 °C range was related to $(Mg,Ni)_2SiO_4$ (COD ID 900053578) forsterite crystallization. The effect was very sensitive to the Ni content: its increase hindered crystallization of the silicate phase or even cancelled it at $x = 1$. PXRD analysis (Figure 3.e) showed that there was an admixture of $(Mg,Ni)SiO_3$ (COD ID 154855179) enstatite, which could crystallize at temperature higher than 1000 °C. Exo-effect of this process should be very weak because the stoichiometry of the system treated in air lies far beyond Mg:Si=1:1 favorable for $MgSiO_3$ formation. Nanocrystalline NiO (COD ID 101038180) was formed instead of forsterite-like phase with very weak exo-effect at 1020 °C in case $x = 1$. This effect could also be attributed to α - SiO_2 crystallization, but this phase was hardly visible on the PXRD pattern. (Figure 3.e) All samples contained amorphous phase, most likely, SiO_2 together with crystalline phases.

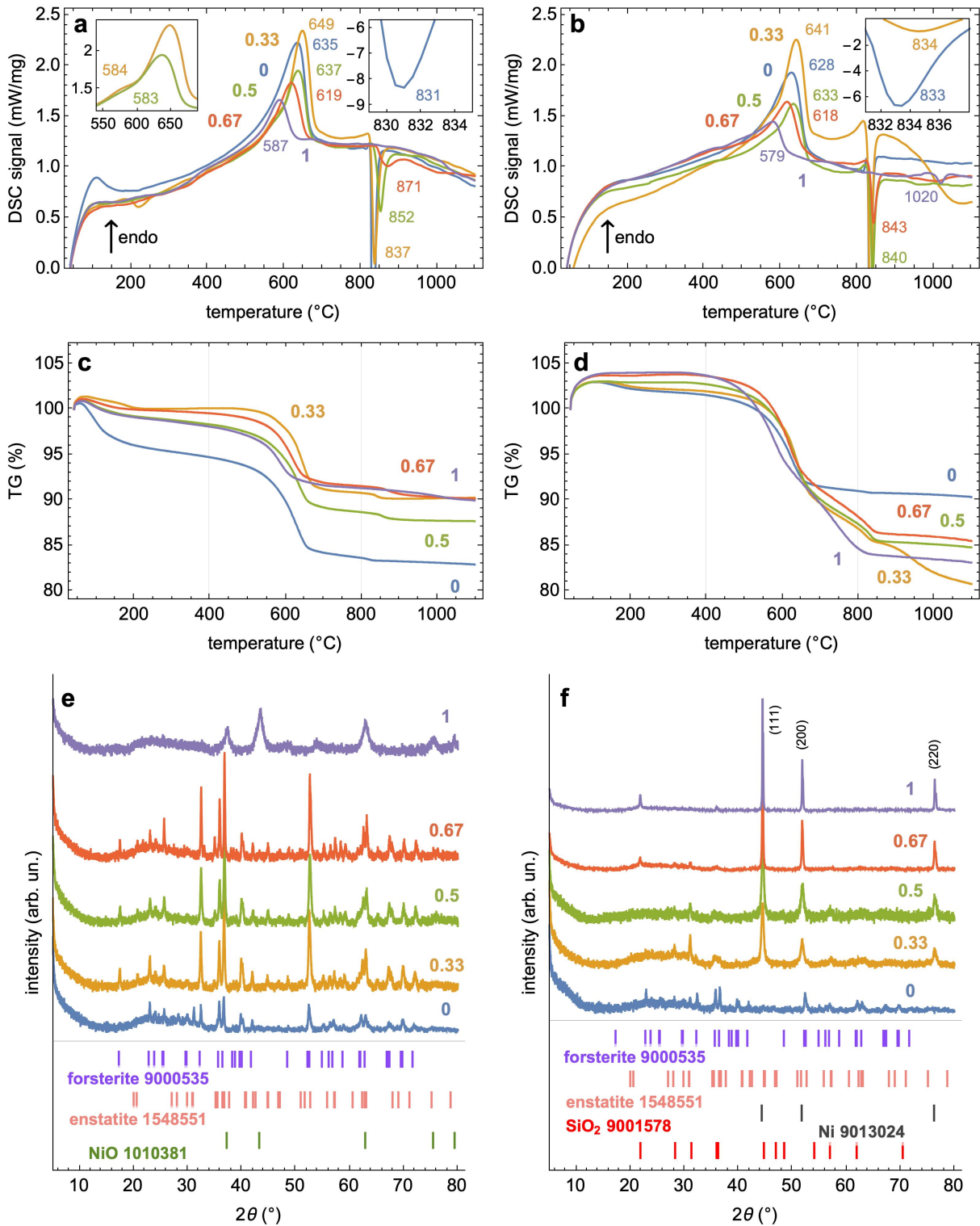


Figure 3. DSC curves obtained (a) in air and (b) in H₂-Ar atmosphere. TG curves obtained (c) in air and (d) in H₂-Ar atmosphere. PXRD patterns obtained after thermal analysis (e) in air and (f) in H₂-Ar atmosphere.

Heat treatment in H₂-Ar

Heat treatment in H₂-Ar mixture (Figure 3.b,d) was accompanied by Ni²⁺ cations reduction. It was assumed that the reduction reaction was slightly exothermic by the analogy with NiO reduction.⁸¹ This process perturbed heat effects curves with weak and hardly visible exo-effects. Only some of them

could be successfully correlated with hydrogen consumption profiles presented in Figure 4. However, the effect of Ni reduction was distinctly seen by an almost two-fold increase in mass loss in the 400-800 °C range. Hydrogen treatment extracted nickel out from the oxide part of the system thus decreasing the metal to silicon ratio.

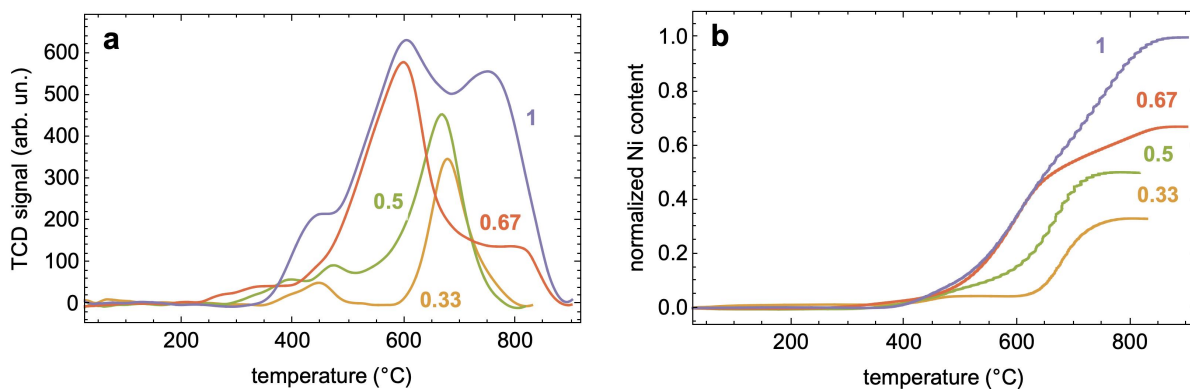


Figure 4. (a) H₂ consumption profiles obtained by the TPR method and (b) cumulative H₂ consumption profiles showing relative quantity of Ni being reduced at certain temperature.

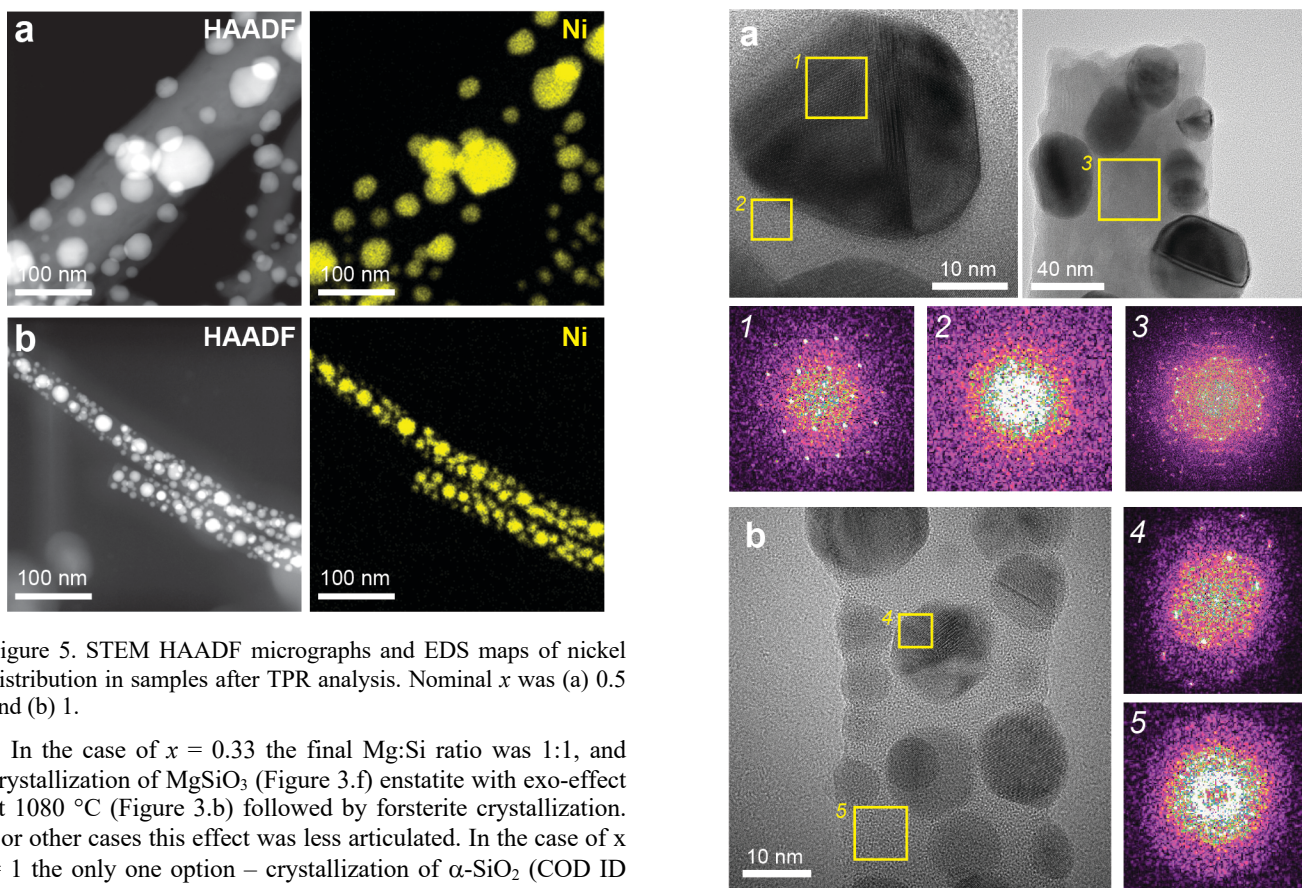


Figure 5. STEM HAADF micrographs and EDS maps of nickel distribution in samples after TPR analysis. Nominal x was (a) 0.5 and (b) 1.

In the case of $x = 0.33$ the final Mg:Si ratio was 1:1, and crystallization of MgSiO₃ (Figure 3.f) enstatite with exo-effect at 1080 °C (Figure 3.b) followed by forsterite crystallization. For other cases this effect was less articulated. In the case of $x = 1$ the only one option – crystallization of α -SiO₂ (COD ID 900157882) – could cause weak exo-effect at 1020 °C.

The reduction of Ni began after 300 °C in a stepwise manner. (Figure 4) At $x = 0.33$, there were two distinct regions of reduction with maxima at 400 °C, 445 °C, and 677 °C with a gap between them where almost no H₂ consumption occurred. Temperature range of this gap coincided with the chrysotile-to-sepiolite transition. (Figure 3.b and Table 2) In contrast to 1:1 sheet arrangement in chrysotile, sepiolite is 2:1 phyllosilicate (Figure S1), in which tetrahedral sheets surround octahedral ones from both sides.^{10,83} This feature could serve as sterical hindrance for the reduction process and grant an increased thermal stability to those Ni cations that had not been reduced. In addition, sepiolite layers were surrounded by Mg-rich amorphous substance, which should be produced due to stoichiometry requirements.

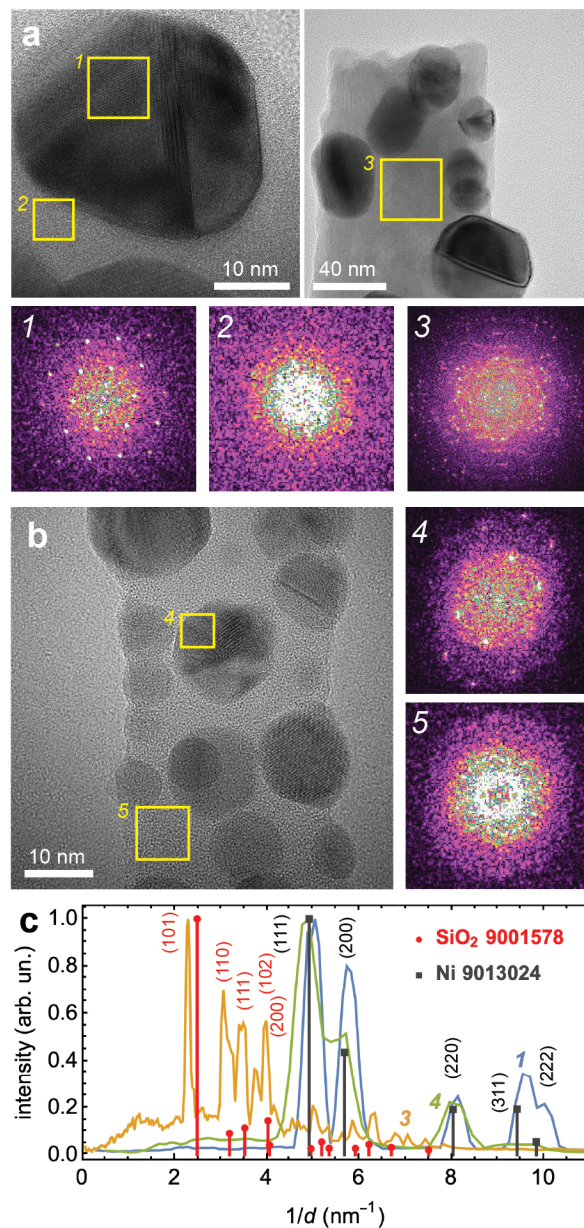


Figure 6. TEM micrographs of TPR products with nominal x (a) 0.5 and (b) 1 with FFT images of selected areas. (c) FFT profiles of selected areas after radial integration.

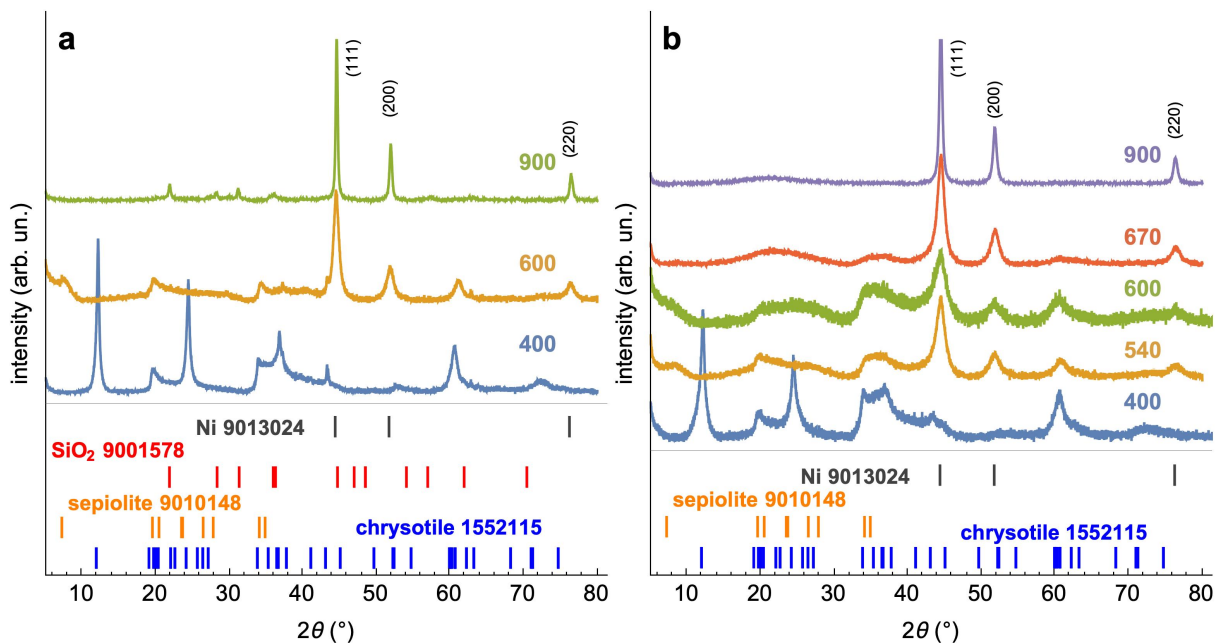


Figure 7. PXRD patterns of Mg-Ni-nanoscrolls with $x =$ (a) 0.67 and (b) 1 reduced in pure H_2 at given temperatures.

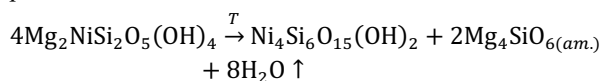
Table 2. Thermal effects in $(Mg_{1-x}Ni_x)_3Si_2O_5(OH)_4$ nanoscrolls in the 100-1100 °C range.

T range, °C	x	mass loss, %	T_{max} of the effect, °C	assignment
100-400	0	3-4; 2 (h)		
	0.33	1-2; 1-2 (h)	–	Removal of adsorbed water, dehydroxylation
	0.5	2; <1 (h)		
			340 (tpr)	Ni reduction in chrysotile layers
			390 (tpr)	
	0.67	1-2; <1 (h)	–	Removal of adsorbed water, dehydroxylation
			274 (tpr)	Ni reduction in chrysotile layers. Probably, reduction of $Ni(OH)_2$ byproduct
			335 (tpr)	
	1	2; <1 (h)	–	Removal of adsorbed water, dehydroxylation
	400-800	0	11; 11 (h)	628 m. en. (h)
			635 m. en.	
0.33		9; 16 (h)	400 (tpr)	Ni reduction in chrysotile layers
			445 (tpr)	
			579 sh. w. en. (h)	Chrysotile-to-sepiolite transition of Ni-rich part
			584 sh. w. en.	
			641 m. en. (h)	Chrysotile-to-sepiolite transition of Mg-rich part
			649 m. en.	
			677 (tpr)	Ni reduction during and after the transition
0.5		9; 16 (h)	472 (tpr)	Ni reduction in chrysotile layers
			579 sh. w. en. (h)	Chrysotile-to-sepiolite transition of Ni-rich part
			583 sh. w. en.	
			633 m. en. (h)	Chrysotile-to-sepiolite transition of Mg-rich part
			637 m. en.	
			667 (tpr)	Ni reduction of amorphous phase formed during the chrysotile-to sepiolite transition
0.67		8; 16 (h)	449 (tpr)	Ni reduction in chrysotile layers
			596 (tpr)	Ni reduction of amorphous phase formed during the

				chrysotile-to sepiolite transition
			618 m. en. (h)	Chrysotile-to-sepiolite transition
			619 m. en.	Ni reduction of amorphous phase formed during sepiolite dehydroxylation
			790 (tpr)	Ni reduction in chrysotile layers
1	7; 20 (h)		447 (tpr)	Chrysotile-to-sepiolite transition
			579 w. en. (h)	
			587 w. en.	Ni reduction of amorphous phase formed during the chrysotile-to sepiolite transition
			600 (tpr)	Ni reduction of amorphous phase formed during sepiolite dehydroxylation
			790 (tpr)	
800-1100	0	1; <1 (h)	831 s. ex.	
			833 s. ex. (h)	Forsterite crystallization
	0.33	1; 6 (h)	834 s. ex. (h)	
			837 m. ex.	
			1080 m. ex. (h)	$\text{Mg}_2\text{SiO}_4 + \text{SiO}_2 \rightarrow 2\text{MgSiO}_3$
	0.5	1; 4 (h)	840 s. ex. (h)	Forsterite crystallization
			852 m. ex.	
			970 v.w. ex. (h)	Enstatite and/or SiO_2 crystallization
			1075 v.w. ex. (h)	
	0.67	1; 3 (h)	843 m. ex. (h)	Forsterite crystallization, probably, still doped by residual Ni^{2+}
			871 w. ex.	Mg-Ni-forsterite crystallization
			950 w. ex. (h)	Enstatite and/or SiO_2 crystallization
			1008 w. ex. (h)	
			1008 sh. v.w. ex.	Enstatite and/or SiO_2 crystallization
			1040 v.w. ex.	
	1	1-2; 2 (h)	1020 w. ex. (h)	SiO_2 crystallization
			1020 v.w. ex.	NiO and/or SiO_2 crystallization

x is nominal Ni content; T_{\max} is temperature of the peaks extremum; (h) points that the value was obtained in the H_2 -Ar atmosphere; (tpr) means that the value was obtained on the basis of the TPR experiment. (Figure 4) Relative intensities of the thermal effects are denoted as follows: ‘v.w.’ – very weak, ‘w.’ – weak, ‘m.’ – medium, ‘s.’ – strong. The effect’s type is denoted as follows: ‘en.’ – endothermic, ‘ex.’ – exothermic. Other designations are: ‘sh.’ – shoulder of the main peak.

In fact, among the samples studied the chrysotile-to-sepiolite transition could be possible without segregation of Ni into the amorphous only for $x = 0.33$, in an extreme case. In terms of metal to silicon ratio the transition is the ratio change from 3:2 to 2:3, or 6:4 $\text{Me}_6\text{Si}_4\text{O}_{10}(\text{OH})_8$ chrysotile-like to sepiolite-like 4:6 $\text{Me}_4\text{Si}_6\text{O}_{15}(\text{OH})_2$. To accomplish this transition, a phase with the 4:1 ratio has to be withdrawn:



Potentially, all nickel cations could be preserved in the sepiolite-like phase only in case $x \leq 0.33$ or else they would end up in the amorphous 4:1 phase and would be reduced immediately. At $x = 0.5$, the reduction process did not disrupt namely because the amorphous 4:1 phase contained sufficient amount of Ni cations. With further increase in the x value up to 0.67 and 1 the beginning of chrysotile-to-sepiolite transition and amorphization, on the contrary, acted like a driver for reduc-

tion. Finally, in these cases high temperature peaks of reduction appeared (Figure 4), which were attributed to Ni reduction in bulk sepiolite-like phase or to amorphous phase formed right after continuous dehydroxylation of sepiolite-like phase. The results of heat effects assignments are summarized in Table 2.

Structure and morphology of Ni-containing composites

Thermal analysis demonstrated the possibility of metallic Ni particles formation from the nanoscrolls by H_2 treatment. TPR (Figure 4) and STEM/EDS analysis of the products (Figure 5) showed that Ni could be completely extracted at high temperature. Nickel nanoparticles were embedded in residual matrix (Figure 6) consisting of amorphous silica or combination of silica and forsterite depending on presence of magnesium cations. General cylindrical morphology of the composite was preserved; however, the inner channel was eliminated completely at high temperature.

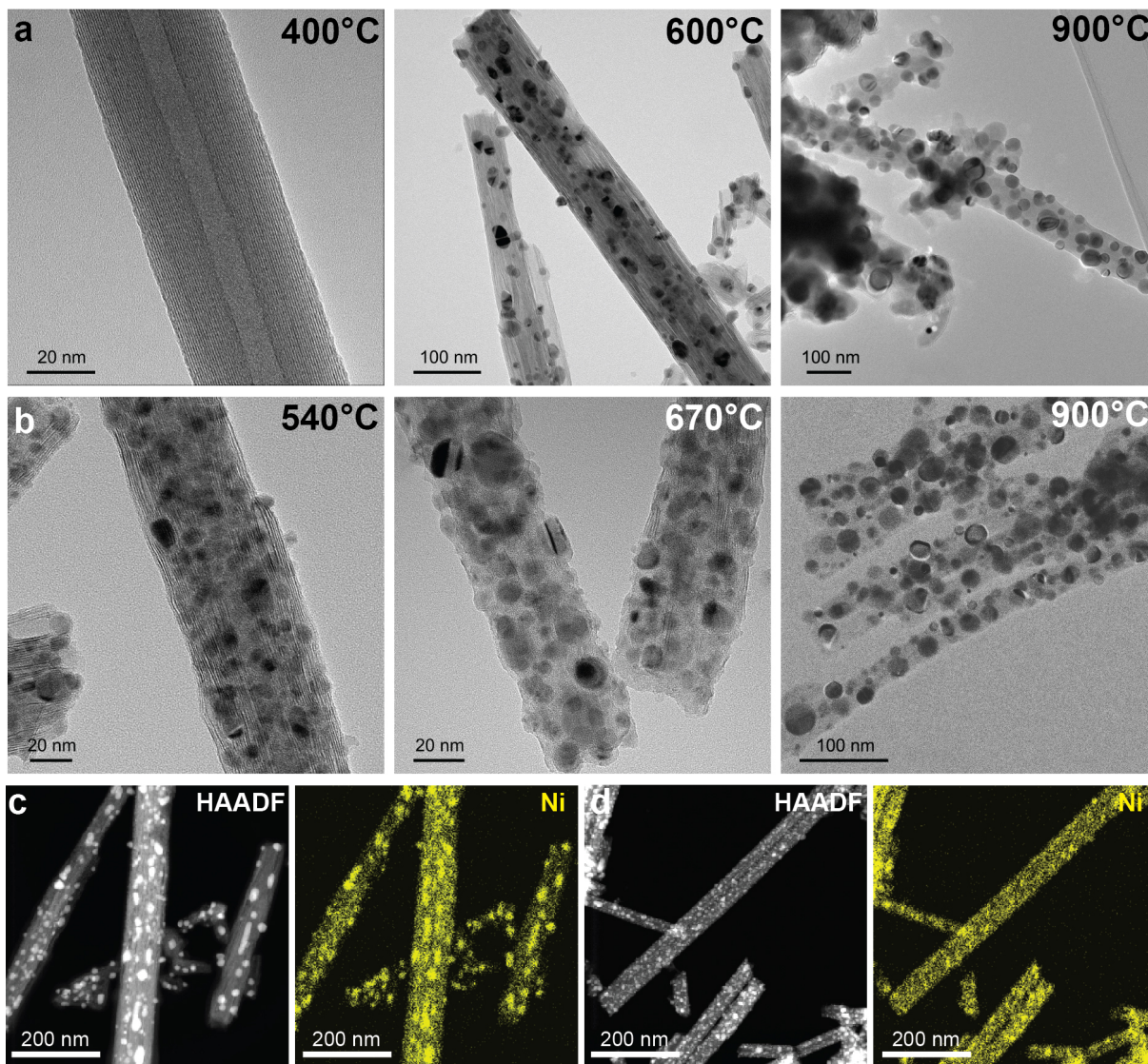


Figure 8. TEM micrographs of Mg-Ni-nanoscrolls with (a) $x = 0.67$ and (b) 1 reduced at certain temperatures. HAADF image and Ni EDS map of Mg-Ni nanoscrolls with (c) $x = 0.67$ reduced at 600 °C and (d) $x = 1$ reduced at 540 °C showing partial Ni reduction.

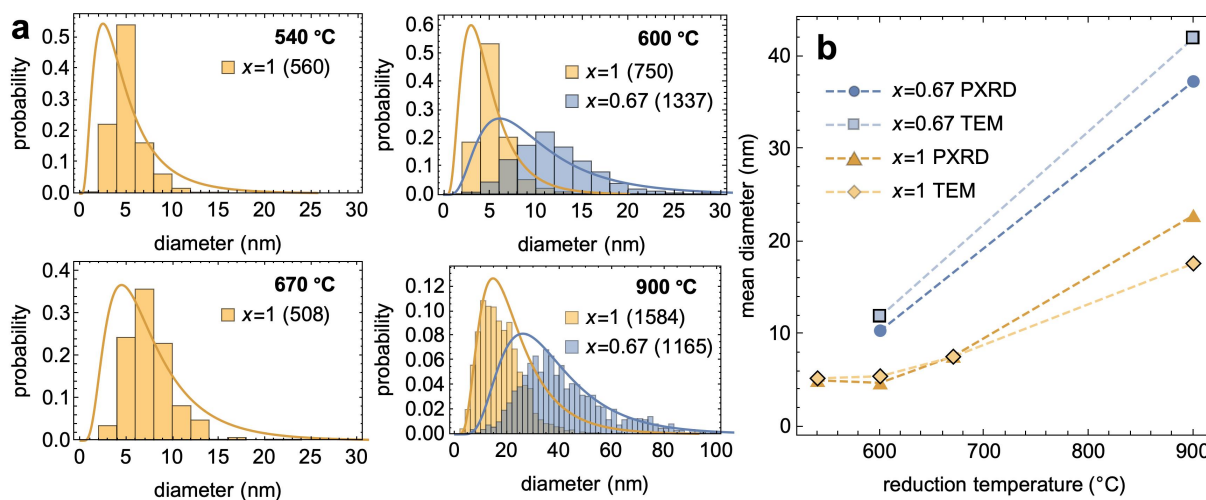


Figure 9. (a) PXR (solid line) and TEM (chart) size distributions of Ni nanoparticles. Total number of the particles measured is given in brackets. (b) Weighted mean diameter of the nanoparticles according to PXR and TEM analysis.

Figure 7 shows PRXD patterns of the samples with highest Ni content ($x = 0.67, 1$), reduced by pure H_2 at given temperatures. Besides TPR (Figure 4) showed start of reduction process at 400 °C, it was complicated to confirm it by PXRD or TEM. Reliable presence of Ni nanoparticles (COD ID 901302484) was found in the samples treated at 540-600 °C. Crystal structure of the nanoscrolls first also changed to sepiolite-like phase (COD ID 901014883) with temperature increase (Figure 7) and then eliminated gradually.

Figure 8 shows degradation of the nanoscroll layered structure and its transformation to composite material. In the first step, hydrosilicate layers thickened and lost their periodicity. In hydrogen atmosphere this process came along with growth of Ni nanoparticles. Further decomposition of the layers yielded amorphous substance, and its subsequent crystallization depended on the initial chemical composition. (Figure 6)

Figure 9 compares PXRD and TEM size distributions of Ni nanoparticles. Generally, Ni particles size distributions broadened, and their weighted average value grew with the temperature increase. Both types of distributions were in a good agreement with each other. Decrease in Ni content yielded increase in Ni particles size, which could be clearly seen in the high temperature region. This feature could be the consequence not only of the higher nucleation speed in the Ni-rich system but also of but also of the crystallization of residual matrix components that try to take room for themselves, force out Ni particles and move them closer to each other. On the other hand, presence of amorphous phase like SiO_2 usually hindered the mass transfer and crystallization of any other component in the system up to high temperature of 1500 °C.⁸⁵

Hydrogenation performance

Figure 10 demonstrates change in BET surface area with increase in H_2 treatment temperature. Decrease in surface area occurred in same manner as it was shown before for the case of $Ni_3Si_2O_5(OH)_4$ nanoscrolls treated in air.³⁸ The decrease had Z-form curve with slight value recovery in the area of chrysotile-to-sepiolite transition. This recovery could be related with features in the nanoscrolls wall alteration (Figure 8) as a kind of thickening and exfoliation of the layers, which could open additional sites for adsorption. The sample with nominal $x = 0.67$ suffered greatly from the heat action probably because of its partial crystallization in the high temperature range. (Figure 7.a)

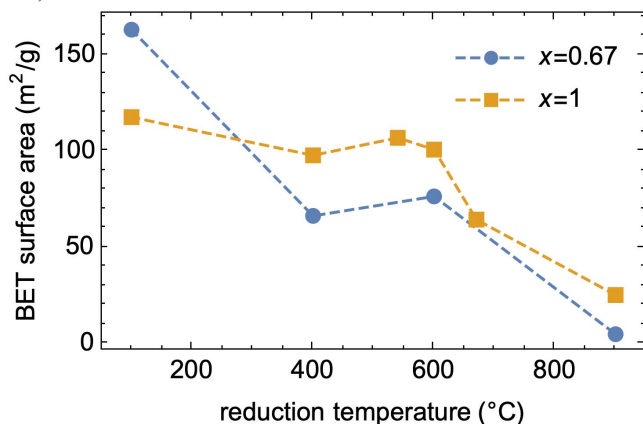


Figure 10. BET surface area of initial nanoscrolls (heat treated in vacuum at 110 °C) and the reduced samples.

Table 3 shows hexane and isopropanol content W after hexene-1 and acetone hydrogenation at two temperatures. Attempts to hydrogenate benzene also have been carried out, but without success: conversion efficiency did not climb over 2%. Both series of samples demonstrated high performance in hydrogenation of hexene-1. The effect took place even in case of samples treated at 400 °C, that indirectly confirms the presence of Ni nanoparticles. These facts are in a good agreement with the literature data. Mokhov et al.⁸⁶ revealed that Ni nanoparticles were an effective catalyst for alkene-into-alkane transformation under mild conditions. Moreover, such catalysts were selective and did not lead to reduction of arenes.

Table 3. Product (hexane or isopropanol) content W (at.%) depending on Ni content and nanoscrolls reduction temperature.

x	$T, ^\circ C$	hexene-1		acetone	
		120 °C	240 °C	120 °C	240 °C
1	400	100	100	71	13
	600	100	100	79	27
	900	100	63	45	14
0.67	400	-	-	23	8
	900	100	100	45	15
0.67	600	100	100	45	15
	900	100	50	20	12

The W value decreased with an increase in the reaction temperature. One of the reasons could be the hydrogenation-dehydration of acetone, as it was shown for the cases with Ni/zeolite⁸⁷ and Ni/ SiO_2 ⁸⁸ catalysts. In particular, Sooknoi et al.⁸⁸ revealed that dehydration rate increased, that lowered the isopropanol content in the products mixture, significantly above 150 °C. This process involves two sequential reactions – hydrogenation of initial acetone to iso-propanol over metal sites of catalyst and dehydration of the alcohol over SiO_2 (or zeolite) sites. Thus, propene could be one of possible dehydration products. The selected experimental conditions and research methods did not allow to capture propene in the reaction products because of its -47.7 °C boiling temperature. So, the observed W value decrease could be assigned to the formation of propene instead of isopropanol at 240°C.

Overall drop of the W value with H_2 treatment temperature increase from 400 °C to 900 °C was likely related to decrease in specific surface area and Ni nanoparticles growth. An increase of the W value with increase in Ni content was related to the particle size decrease, i.e. to increase their surface-to-volume ratio. Accumulative H_2 consumption profiles (Figure 4.b) showed that at any temperature lower than 650 °C equal quantities of Ni have been reduced in samples with $x = 0.67$ and 1. Assuming spherical form of Ni nanoparticles, the surface-to-volume ratio could be written as follows:

$$s = \pi d^2 \left(\frac{4}{3} \pi \frac{d^3}{8} \right)^{-1} = \frac{6}{d} \quad (1)$$

where d is a weighted average diameter.

Relative change of a value v was written as follows:

$$\Delta v = \frac{|v_{0.67} - v_1|}{\text{Max}(v_{0.67}, v_1)} 100\% \quad (2)$$

where lower index means nominal Ni content.

These two equations were applied to weighted average diameter (Figure 9.b) and W value (Table 3) of the samples reduced at 600 °C and used as acetone hydrogenation catalysts at 120 °C. It was found that $\Delta S_{600} = 54\%$ and $\Delta W_{600} = 43\%$. In the case samples were reduced at 900 °C, the equations yielded $\Delta S_{900} = 58\%$ and $\Delta W_{900} = 56\%$. The proximity of these two values spoke in favor of the decisive role of the particles surface-to-volume ratio in the hydrogenation process.

CONCLUSIONS

Here we considered chemical and structural transformations occurring in $(\text{Mg}_{1-x}\text{Ni}_x)_3\text{Si}_2\text{O}_5(\text{OH})_4$ nanoscrolls, obtained by hydrothermal synthesis, under heating in air and in H_2 -Ar flow. In air, the nanoscrolls passed through a number of dehydroxylation steps with endothermic transition to a sepiolite-like phase in the 580-650 °C range following by exothermic silicate, silica, or nickel oxide crystallization depending on the initial chemical composition. In H_2 -Ar, nickel can be fully or partially reduced out from nanoscrolls in a tunable manner. The reduction process overlapped with endothermic dehydroxylation stages and did not show obvious thermal effects even though it was distinctly detected on the TG curves. Transition to sepiolite-like phase influenced on the reduction process by sealing up a part of nickel-containing octahedrons cations with SiO_2 sheets from both sides. This feature modulated the shape of H_2 consumption profiles resulting in appearance of gaps and peak splitting. Mean diameter of Ni nanoparticles obtained by the reduction decreased with increase of Ni content in the initial nanoscrolls, that was attributed to increase in nucleation rate and quantity of amorphous phase, which hindered mass transfer between Ni nanoparticles at high temperature. Difference in the size-to-volume ratio of Ni nanoparticles distribution, as well as specific surface area decrease during heat treatment, produced an optimal 600 °C reduction temperature in the view of the hydrogenation conversion rate.

ASSOCIATED CONTENT

Supporting Information

The Supporting Information is available free of charge on the ACS Publications website.

Crystal structures of chrysotile and sepiolite (PDF)

AUTHOR INFORMATION

Corresponding Author

*E-mail: ikrasilin@mail.ioffe.ru

Author Contributions

The manuscript was written through contributions of all authors. All authors have given approval to the final version of the manuscript.

ACKNOWLEDGMENT

The research was partially supported by the Russian Science Foundation (Grant 19-13-00151). A.N., S.B. and J.G. are thankful to the French Ministry of Higher Education, Research and Innovation for financial support through Program Hubert Curien-Kolmogorov. A.N. is thankful to "ITMO Fellowship and Professorship" program. X-ray studies were carried out on the equipment of the Engineering Center of Saint-Petersburg State Technological Institute (Technical University). The authors would like to

thank E.V. Kryachko, K.I. Timoschuk, D.P. Danilovich, and Prof. V.V. Gusarov for assistance and fruitful discussions.

ABBREVIATIONS

TPR, temperature-programmed reduction; DSC, differential scanning calorimetry; TG, thermogravimetry; NMR, nuclear magnetic resonance; PXRD, powder X-ray diffraction; COD, Crystallography Open Database; SEM, scanning electron microscopy; TEM, transmission electron microscopy; STEM, scanning transmission electron microscopy; EDS, energy dispersive X-ray spectroscopy; HAADF, high-angle annular dark field; FFT, fast Fourier transform; BET, Brunauer-Emmett-Teller; .

REFERENCES

- (1) Krasilin, A. A.; Nevedomsky, V. N.; Gusarov, V. V. Comparative Energy Modeling of Multiwalled $\text{Mg}_3\text{Si}_2\text{O}_5(\text{OH})_4$ and $\text{Ni}_3\text{Si}_2\text{O}_5(\text{OH})_4$ Nanoscroll Growth. *J. Phys. Chem. C* **2017**, *121*, 12495–12502. <https://doi.org/10.1021/acs.jpcc.7b03785>.
- (2) Guimarães, L.; Enyashin, A. N.; Seifert, G.; Duarte, H. A. Structural, Electronic, and Mechanical Properties of Single-Walled Halloysite Nanotube Models. *J. Phys. Chem. C* **2010**, *114*, 11358–11363. <https://doi.org/10.1021/jp100902e>.
- (3) Thill, A.; Guiose, B.; Bacia-Verloop, M.; Geertsen, V.; Belloni, L. How the Diameter and Structure of $(\text{OH})_3\text{Al}_2\text{O}_3\text{Si}_x\text{Ge}_{1-x}\text{OH}$ Imogolite Nanotubes Are Controlled by an Adhesion versus Curvature Competition. *J. Phys. Chem. C* **2012**, *116*, 26841–26849. <https://doi.org/10.1021/jp310547k>.
- (4) Dódony, I.; Buseck, P. R. Serpentine Close-Up and Intimate: An HRTEM View. *Int. Geol. Rev.* **2004**, *46*, 507–527. <https://doi.org/10.2747/0020-6814.46.6.507>.
- (5) Shchupalov, Y. K. Surface Energy of Crystalline and Vitreous Silica. *Glas. Ceram.* **2000**, *57*, 374–377. <https://doi.org/10.1023/A:101090093019>.
- (6) Evarestov, R. A.; Bandura, A. V. HF and DFT Calculations of MgO Surface Energy and Electrostatic Potential Using Two- and Three-Periodic Models. *Int. J. Quantum Chem.* **2004**, *100*, 452–459. <https://doi.org/10.1002/qua.20188>.
- (7) Churakov, S. V.; Iannuzzi, M.; Parrinello, M. Ab Initio Study of Dehydroxylation–Carbonation Reaction on Brucite Surface. *J. Phys. Chem. B* **2004**, *108*, 11567–11574. <https://doi.org/10.1021/jp037935x>.
- (8) Bloise, A.; Catalano, M.; Barrese, E.; Gualtieri, A. F.; Bursi Gandolfi, N.; Capella, S.; Belluso, E. TG/DSC Study of the Thermal Behaviour of Hazardous Mineral Fibres. *J. Therm. Anal. Calorim.* **2016**, *123*, 2225–2239. <https://doi.org/10.1007/s10973-015-4939-8>.
- (9) Joussein, E.; Petit, S.; Churchman, J.; Theng, B.; Righi, D.; Delvaux, B. Halloysite Clay Minerals — a Review. *Clay Miner.* **2005**, *40*, 383–426. <https://doi.org/10.1180/0009855054040180>.
- (10) Falini, G.; Foresti, E.; Gazzano, M.; Gualtieri, A. F.; Leoni, M.; Lesci, I. G.; Roveri, N. Tubular-Shaped Stoichiometric Chrysotile Nanocrystals. *Chemistry* **2004**, *10*, 3043–3049. <https://doi.org/10.1002/chem.200305685>.
- (11) Lafay, R.; Fernandez-Martinez, A.; Montes-Hernandez, G.; Auzende, A. L.; Poulain, A. Dissolution-Recipitation and Self-Assembly of Serpentine Nanoparticles Preceding Chrysotile Formation: Insights into the Structure of Proto-Serpentine. *Am. Mineral.* **2016**, *101*, 2666–2676. <https://doi.org/10.2138/am-2016-5772>.
- (12) Korytkova, E. N.; Brovkin, A. S.; Maslennikova, T. P.; Pivovarova, L. N.; Drozdova, I. A. Influence of the Physicochemical Parameters of Synthesis on the Growth of Nanotubes of the $\text{Mg}_3\text{Si}_2\text{O}_5(\text{OH})_4$ Composition under Hydrothermal Conditions. *Glas. Phys. Chem.* **2011**, *37*, 161–171. <https://doi.org/10.1134/S1087659611020076>.
- (13) Krasilin, A. A.; Almjashahe, O. V.; Gusarov, V. V. Effect of the Structure of Precursors on the Formation of Nanotubular Magnesium Hydrosilicate. *Inorg. Mater.* **2011**, *47*, 1111–1115. <https://doi.org/10.1134/S002016851110013X>.

- (14) Bloise, A.; Belluso, E.; Catalano, M.; Barrese, E.; Miriello, D.; Apollaro, C. Hydrothermal Alteration of Glass to Chrysotile. *J. Am. Ceram. Soc.* **2012**, *95*, 3050–3055. <https://doi.org/10.1111/j.1551-2916.2012.05323.x>.
- (15) Bloise, A.; Belluso, E.; Barrese, E.; Miriello, D.; Apollaro, C. Synthesis of Fe-Doped Chrysotile and Characterization of the Resulting Chrysotile Fibers. *Cryst. Res. Technol.* **2009**, *44*, 590–596. <https://doi.org/10.1002/crat.200900135>.
- (16) Krasilin, A. A.; Panchuk, V. V.; Semenov, V. G.; Gusarov, V. V. Formation of Variable-Composition Iron(III) Hydrosilicates with the Chrysotile Structure. *Russ. J. Gen. Chem.* **2016**, *86*, 2581–2588. <https://doi.org/10.1134/S1070363216120021>.
- (17) Ogorodova, L. P.; Kiseleva, I. A.; Korytkova, E. N.; Maslennikova, T. P.; Gusarov, V. V. The Synthesis and Thermochemical Study of $(\text{Mg,Fe})_3\text{Si}_2\text{O}_5(\text{OH})_4$ Nanotubes. *Russ. J. Phys. Chem. A* **2010**, *84*, 44–47. <https://doi.org/10.1134/S0036024410010097>.
- (18) Korytkova, E. N.; Pivovarova, L. N.; Drosdova, I. A.; Gusarov, V. V. Hydrothermal Synthesis of Nanotubular Co-Mg Hydrosilicates with the Chrysotile Structure. *Russ. J. Gen. Chem.* **2007**, *77*, 1669–1676. <https://doi.org/10.1134/S1070363207100039>.
- (19) Park, J. C.; Kang, S. W.; Kim, J.-C.; Kwon, J. I.; Jang, S.; Rhim, G. B.; Kim, M.; Chun, D. H.; Lee, H.-T.; Jung, H.; Song, H.; Yang, J.-I. Synthesis of Co/SiO_2 Hybrid Nanocatalyst via Twisted $\text{Co}_3\text{Si}_2\text{O}_5(\text{OH})_4$ Nanosheets for High-Temperature Fischer–Tropsch Reaction. *Nano Res.* **2017**, *10*, 1044–1055. <https://doi.org/10.1007/s12274-016-1364-7>.
- (20) Korytkova, E. N.; Maslov, A. V.; Pivovarova, L. N.; Polegotchenkova, Y. V.; Povnich, V. F.; Gusarov, V. V. Synthesis of Nanotubular $\text{Mg}_3\text{Si}_2\text{O}_5(\text{OH})_4$ - $\text{Ni}_3\text{Si}_2\text{O}_5(\text{OH})_4$ Silicates at Elevated Temperatures and Pressures. *Inorg. Mater.* **2005**, *41*, 743–749. <https://doi.org/10.1007/s10789-005-0202-1>.
- (21) McDonald, A.; Scott, B.; Villemure, G. Hydrothermal Preparation of Nanotubular Particles of a 1:1 Nickel Phyllosilicate. *Microporous Mesoporous Mater.* **2009**, *120*, 263–266. <https://doi.org/10.1016/j.micromeso.2008.11.013>.
- (22) Bloise, A.; Belluso, E.; Formero, E.; Rinaudo, C.; Barrese, E.; Capella, S. Influence of Synthesis Conditions on Growth of Ni-Doped Chrysotile. *Microporous Mesoporous Mater.* **2010**, *132*, 239–245. <https://doi.org/10.1016/j.micromeso.2010.03.003>.
- (23) Maslennikova, T. P.; Korytkova, E. N. Influence of Synthesis of Physicochemical Parameters on Growth of $\text{Ni}_3\text{Si}_2\text{O}_5(\text{OH})_4$ Nanotubes and Their Filling with Solutions of Hydroxides and Chlorides of Alkaline Metals. *Glas. Phys. Chem.* **2013**, *39*, 67–72. <https://doi.org/10.1134/S1087659613010082>.
- (24) Yang, Y.; Liang, Q.; Li, J.; Zhuang, Y.; He, Y.; Bai, B.; Wang, X. $\text{Ni}_3\text{Si}_2\text{O}_5(\text{OH})_4$ Multi-Walled Nanotubes with Tunable Magnetic Properties and Their Application as Anode Materials for Lithium Batteries. *Nano Res.* **2011**, *4*, 882–890. <https://doi.org/10.1007/s12274-011-0144-7>.
- (25) White, R. D.; Bavykin, D. V.; Walsh, F. C. Morphological Control of Synthetic $\text{Ni}_3\text{Si}_2\text{O}_5(\text{OH})_4$ Nanotubes in an Alkaline Hydrothermal Environment. *J. Mater. Chem. A* **2013**, *1*, 548–556. <https://doi.org/10.1039/c2ta00257d>.
- (26) Bian, Z.; Li, Z.; Ashok, J.; Kawi, S. A Highly Active and Stable Ni–Mg Phyllosilicate Nanotubular Catalyst for Ultrahigh Temperature Water-Gas Shift Reaction. *Chem. Commun.* **2015**, *51*, 16324–16326. <https://doi.org/10.1039/C5CC05226B>.
- (27) Krasilin, A. A.; Khrapova, E. K.; Nominé, A.; Ghanbaja, J.; Belmonte, T.; Gusarov, V. V. Cation Redistribution along the Spiral of Ni-Doped Phyllosilicate Nanoscrolls: Energy Modelling and STEM/EDS Study. *ChemPhysChem* **2019**, *20*, 719–726. <https://doi.org/10.1002/cphc.201801144>.
- (28) Bloise, A.; Barrese, E.; Apollaro, C. Hydrothermal Alteration of Ti-Doped Forsterite to Chrysotile and Characterization of the Resulting Chrysotile Fibers. *Neues Jahrb. für Mineral. - Abhandlungen* **2009**, *185*, 297–304. <https://doi.org/10.1127/0077-7757/2009/0130>.
- (29) Maslennikova, T. P.; Gatina, E. N. Hydrothermal Synthesis of Ti-Doped Nickel Hydrosilicates of Various Morphologies. *Appl. Chem.* **2018**, *91*, 286–291. <https://doi.org/10.1134/S1070427218020179>.
- (30) White, R. D.; Bavykin, D. V.; Walsh, F. C. Spontaneous Scrolling of Kaolinite Nanosheets into Halloysite Nanotubes in an Aqueous Suspension in the Presence of GeO_2 . *J. Phys. Chem. C* **2012**, *116*, 8824–8833. <https://doi.org/10.1021/jp300068t>.
- (31) Perbost, R.; Amouric, M.; Olives, J. Influence of Cation Size on the Curvature of Serpentine Minerals: Hrtem-Aem Study and Elastic Theory. *Clays Clay Miner.* **2003**, *51*, 430–438. <https://doi.org/10.1346/CCMN.2003.0510409>.
- (32) Krasilin, A. A.; Khrapova, E. K. Effect of Hydrothermal Treatment Conditions on Formation of Nickel Hydrogermanate with Platy Morphology. *Russ. J. Appl. Chem.* **2017**, *90*, 22–27. <https://doi.org/10.1134/S1070427217010049>.
- (33) Piperno, S.; Kaplan-Ashiri, I.; Cohen, S. R.; Popovitz-Biro, R.; Wagner, H. D.; Tenne, R.; Foresti, E.; Lesci, I. G.; Roveri, N. Characterization of Geinspired and Synthetic Chrysotile Nanotubes by Atomic Force Microscopy and Transmission Electron Microscopy. *Adv. Funct. Mater.* **2007**, *17*, 3332–3338. <https://doi.org/10.1002/adfm.200700278>.
- (34) Krasilin, A. A.; Semenov, A. S.; Kellerman, D. G.; Nevedomsky, V. N.; Gusarov, V. V. Magnetic Properties of Synthetic $\text{Ni}_3\text{Si}_2\text{O}_5(\text{OH})_4$ Nanotubes. *EPL (Europhysics Letters)* **2016**, *113*, 47006. <https://doi.org/10.1209/0295-5075/113/47006>.
- (35) Li, X.; Wang, D.; Liu, Q.; Komarneni, S. A. Comparative Study of Synthetic Tubular Kaolinite Nanoscrolls and Natural Halloysite Nanotubes. *Appl. Clay Sci.* **2019**, *168*, 421–427. <https://doi.org/10.1016/j.clay.2018.12.014>.
- (36) Ferrante, F.; Armata, N.; Cavallaro, G.; Lazzara, G. Adsorption Studies of Molecules on the Halloysite Surfaces: A Computational and Experimental Investigation. *J. Phys. Chem. C* **2017**, *121*, 2951–2958. <https://doi.org/10.1021/acs.jpcc.6b12876>.
- (37) Yuan, P.; Tan, D.; Annabi-Bergaya, F. Properties and Applications of Halloysite Nanotubes: Recent Research Advances and Future Prospects. *Appl. Clay Sci.* **2015**, *112–113*, 75–93. <https://doi.org/10.1016/j.clay.2015.05.001>.
- (38) Krasilin, A. A.; Danilovich, D. P.; Yudina, E. B.; Bruyere, S.; Ghanbaja, J.; Ivanov, V. K. Crystal Violet Adsorption by Oppositely Twisted Heat-Treated Halloysite and Pecoraite Nanoscrolls. *Appl. Clay Sci.* **2019**, *173*, 1–11. <https://doi.org/10.1016/j.clay.2019.03.007>.
- (39) Yu, S.; Zhai, L.; Wang, Y.; Liu, X.; Xu, L.; Cheng, L. Synthesis of Magnetic Chrysotile Nanotubes for Adsorption of Pb(II), Cd(II) and Cr(III) Ions from Aqueous Solution. *J. Environ. Chem. Eng.* **2015**, *3*, 752–762. <https://doi.org/10.1016/j.jece.2015.03.023>.
- (40) Bian, Z.; Kawi, S. Preparation, Characterization and Catalytic Application of Phyllosilicate: A Review. *Catal. Today* **2020**, *339*, 3–23. <https://doi.org/10.1016/j.cattod.2018.12.030>.
- (41) Lafay, R.; Montes-Hernandez, G.; Janots, E.; Auzende, A.-L.; Chiriac, R.; Lemarchand, D.; Toche, F. Influence of Trace Elements on the Textural Properties of Synthetic Chrysotile: Complementary Insights from Macroscopic and Nanoscopic Measurements. *Microporous Mesoporous Mater.* **2014**, *183*, 81–90. <https://doi.org/10.1016/j.micromeso.2013.08.032>.
- (42) Belkassa, K.; Bessaha, F.; Marouf-Khelifa, K.; Batonneau-Gener, I.; Comparot, J.; Khelifa, A. Physicochemical and Adsorptive Properties of a Heat-Treated and Acid-Leached Algerian Halloysite. *Colloids Surfaces A Physicochem. Eng. Asp.* **2013**, *421*, 26–33. <https://doi.org/10.1016/J.COLSURFA.2012.12.048>.
- (43) Sivaiah, M. V.; Petit, S.; Beaufort, M. F.; Eyidi, D.; Barrault, J.; Batiot-Dupeyrat, C.; Valange, S. Nickel Based Catalysts Derived from Hydrothermally Synthesized 1:1 and 2:1 Phyllosilicates as Precursors for Carbon Dioxide Reforming of Methane. *Microporous Mesoporous Mater.* **2011**, *140*, 69–80. <https://doi.org/10.1016/J.MICROMESO.2010.09.015>.
- (44) Bian, Z.; Suryawinata, I. Y.; Kawi, S. Highly Carbon Resistant Multicore-Shell Catalyst Derived from Ni-Mg Phyllosilicate Nanotubes@silica for Dry Reforming of Methane. *Appl. Catal. B Environ.* **2016**, *195*, 1–8. <https://doi.org/10.1016/j.apcatb.2016.05.001>.

- (45) Lvov, Y.; Wang, W.; Zhang, L.; Fakhrullin, R. Halloysite Clay Nanotubes for Loading and Sustained Release of Functional Compounds. *Adv. Mater.* **2016**, *28*, 1227–1250. <https://doi.org/10.1002/adma.201502341>.
- (46) Cavallaro, G.; Danilushkina, A.; Evtugyn, V.; Lazzara, G.; Milioto, S.; Parisi, F.; Rozhina, E.; Fakhrullin, R. Halloysite Nanotubes: Controlled Access and Release by Smart Gates. *Nanomaterials* **2017**, *7*, 199. <https://doi.org/10.3390/nano7080199>.
- (47) Mahrez, N.; Bendenia, S.; Marouf-Khelifa, K.; Batonneau-Gener, I.; Khelifa, A. Improving of the Adsorption Capacity of Halloysite Nanotubes Intercalated with Dimethyl Sulfoxide. *Compos. Interfaces* **2015**, *22*, 403–417. <https://doi.org/10.1080/09276440.2015.1036581>.
- (48) Li, X.; QianYang; Ouyang, J.; Yang, H.; Chang, S. Chitosan Modified Halloysite Nanotubes as Emerging Porous Microspheres for Drug Carrier. *Appl. Clay Sci.* **2016**, *126*, 306–312. <https://doi.org/10.1016/j.clay.2016.03.035>.
- (49) Grabka, D.; Raczynska-Żak, M.; Czech, K.; Słomkiewicz, P. M.; Józwiak, M. A. Modified Halloysite as an Adsorbent for Prometryn from Aqueous Solutions. *Appl. Clay Sci.* **2015**, *114*, 321–329. <https://doi.org/10.1016/j.clay.2015.06.012>.
- (50) Zhang, S.; Sheng, Q.; Zheng, J. Synthesis of Au Nanoparticles Dispersed on Halloysite Nanotubes-Reduced Graphene Oxide Nanosheets and Their Application for Nitrites Electrochemical Sensing. *New J. Chem.* **2016**, *40*, 9672–9678. <https://doi.org/10.1039/C6NJ02103D>.
- (51) Krasilin, A. A.; Bodalyov, I. S.; Malkov, A. A.; Khrapova, E. K.; Maslennikova, T. P.; Malygin, A. A. On an Adsorption/Photocatalytic Performance of Nanotubular $\text{Mg}_3\text{Si}_2\text{O}_5(\text{OH})_4/\text{TiO}_2$ Composite. *Nanosyst. Physics, Chem. Math.* **2018**, *9*, 410–416. <https://doi.org/10.17586/2220-8054-2018-9-3-410-416>.
- (52) Carrillo, A. M.; Carriazo, J. G. Cu and Co Oxides Supported on Halloysite for the Total Oxidation of Toluene. *Appl. Catal. B Environ.* **2015**, *164*, 443–452. <https://doi.org/10.1016/j.apcatb.2014.09.027>.
- (53) Vinokurov, V. A.; Stavitskaya, A. V.; Chudakov, Y. A.; Ivanov, E. V.; Shrestha, L. K.; Ariga, K.; Darrat, Y. A.; Lvov, Y. M. Formation of Metal Clusters in Halloysite Clay Nanotubes. *Sci. Technol. Adv. Mater.* **2017**, *18*, 147–151. <https://doi.org/10.1080/14686996.2016.1278352>.
- (54) Zhao, Z.; Ren, P.; Li, W. Supported Ni Catalyst on a Natural Halloysite Derived Silica–Alumina Composite Oxide with Unexpected Coke-Resistant Stability for Steam- CO_2 Dual Reforming of Methane. *RSC Adv.* **2016**, *6*, 49487–49496. <https://doi.org/10.1039/C6RA09203A>.
- (55) Li, C.; Li, X.; Duan, X.; Li, G.; Wang, J. Halloysite Nanotube Supported Ag Nanoparticles Heteroarchitectures as Catalysts for Polymerization of Alkylsilanes to Superhydrophobic Silanol/Siloxane Composite Microspheres. *J. Colloid Interface Sci.* **2014**, *436*, 70–76. <https://doi.org/10.1016/j.jcis.2014.08.051>.
- (56) Zhang, X.; Wang, P.; Wu, X.; Lv, S.; Dai, J. Application of MnO_x /HNTs Catalysts in Low-Temperature NO Reduction with NH_3 . *Catalysis Communications* **2016**, *83*, 18–21. <https://doi.org/10.1016/j.catcom.2016.05.003>.
- (57) Massaro, M.; Riela, S.; Cavallaro, G.; Colletti, C. G.; Milioto, S.; Noto, R.; Parisi, F.; Lazzara, G. Palladium Supported on Halloysite-Triazolium Salts as Catalyst for Ligand Free Suzuki Cross-Coupling in Water under Microwave Irradiation. *J. Mol. Catal. A Chem.* **2015**, *408*, 12–19. <https://doi.org/10.1016/j.molcata.2015.07.008>.
- (58) Barrientos-Ramírez, S.; Ramos-Fernández, E. V.; Silvestre-Albero, J.; Sepúlveda-Escribano, A.; Pastor-Blas, M. M.; González-Montiel, A. Use of Nanotubes of Natural Halloysite as Catalyst Support in the Atom Transfer Radical Polymerization of Methyl Methacrylate. *Microporous Mesoporous Mater.* **2009**, *120*, 132–140. <https://doi.org/10.1016/j.micromeso.2008.08.015>.
- (59) Zhang, C.; Zhu, W.; Li, S.; Wu, G.; Ma, X.; Wang, X.; Gong, J. Sintering-Resistant Ni-Based Reforming Catalysts Obtained via the Nanoconfinement Effect. *Chem. Commun.* **2013**, *49*, 9383–9385. <https://doi.org/10.1039/c3cc43895c>.
- (60) Ashok, J.; Bian, Z.; Wang, Z.; Kawi, S. Ni-Phyllosilicate Structure Derived Ni– SiO_2 – MgO Catalysts for Bi-Reforming Applications: Acidity, Basicity and Thermal Stability. *Catal. Sci. Technol.* **2018**, *8*, 1730–1742. <https://doi.org/10.1039/C7CY02475D>.
- (61) Bian, Z.; Kawi, S. Highly Carbon-Resistant Ni–Co/ SiO_2 Catalysts Derived from Phyllosilicates for Dry Reforming of Methane. *J. CO₂ Util.* **2017**, *18*, 345–352. <https://doi.org/10.1016/J.JCOU.2016.12.014>.
- (62) Yue, H.; Zhao, Y.; Zhao, S.; Wang, B.; Ma, X.; Gong, J. A Copper-Phyllosilicate Core-Sheath Nanoreactor for Carbon–Oxygen Hydrogenolysis Reactions. *Nat. Commun.* **2013**, *4*, No. 2339. <https://doi.org/10.1038/ncomms3339>.
- (63) Wang, X.; Zhu, S.; Wang, S.; Wang, J.; Fan, W.; Lv, Y. Ni Nanoparticles Entrapped in Nickel Phyllosilicate for Selective Hydrogenation of Guaiacol to 2-Methoxycyclohexanol. *Appl. Catal. A Gen.* **2018**, *568*, 231–241. <https://doi.org/10.1016/J.APCATA.2018.10.009>.
- (64) Bian, Z.; Das, S.; Wai, M. H.; Hongmanom, P.; Kawi, S. A Review on Bimetallic Nickel-Based Catalysts for CO_2 Reforming of Methane. *ChemPhysChem* **2017**, *18*, 3117–3134. <https://doi.org/10.1002/cphc.201700529>.
- (65) Ellert, O. G.; Tsodikov, M. V.; Nikolaev, S. A.; Novotortsev, V. M. Bimetallic Nanoalloys in Heterogeneous Catalysis of Industrially Important Reactions: Synergistic Effects and Structural Organization of Active Components. *Russ. Chem. Rev.* **2014**, *83*, 718–732. <https://doi.org/10.1070/RC2014v083n08ABEH004432>.
- (66) Malkov, A. A.; Korytkova, E. N.; Maslennikova, T. P.; Shtykhova, A. M.; Gusarov, V. V. Effect of Heat Treatment on Structural-Chemical Transformations in Magnesium Hydrosilicate $[\text{Mg}_3\text{Si}_2\text{O}_5(\text{OH})_4]$ Nanotubes. *Russ. J. Appl. Chem.* **2009**, *82*, 2079–2086. <https://doi.org/10.1134/S1070427209120015>.
- (67) Foresti, E.; Hochella, M. F.; Kornishi, H.; Lesci, I. G.; Madden, A. S.; Roveri, N.; Xu, H. Morphological and Chemical/Physical Characterization of Fe-Doped Synthetic Chrysotile Nanotubes. *Adv. Funct. Mater.* **2005**, *15*, 1009–1016. <https://doi.org/10.1002/adfm.200400355>.
- (68) Gražulis, S.; Daškevič, A.; Merkys, A.; Chateigner, D.; Lutterotti, L.; Quirós, M.; Serebryanaya, N. R.; Moeck, P.; Downs, R. T.; Le Bail, A. Crystallography Open Database (COD): An Open-Access Collection of Crystal Structures and Platform for World-Wide Collaboration. *Nucleic Acids Res.* **2012**, *40*, D420–D427. <https://doi.org/10.1093/nar/gkr900>.
- (69) Gražulis, S.; Merkys, A.; Vaitkus, A.; Okulič-Kazarinas, M. Computing Stoichiometric Molecular Composition from Crystal Structures. *J. Appl. Crystallogr.* **2015**, *48*, 85–91. <https://doi.org/10.1107/S1600576714025904>.
- (70) Momma, K.; Izumi, F. *VESTA 3* for Three-Dimensional Visualization of Crystal, Volumetric and Morphology Data. *J. Appl. Crystallogr.* **2011**, *44*, 1272–1276. <https://doi.org/10.1107/S0021889811038970>.
- (71) Cheary, R. W.; Coelho, A. A. Fundamental Parameters Approach to X-Ray Line-Profile Fitting. *J. Appl. Crystallogr.* **1992**, *25*, 109–121. <https://doi.org/10.1107/S0021889891010804>.
- (72) Le Bail, A. Whole Powder Pattern Decomposition Methods and Applications: A Retrospection. *Powder Diffr.* **2005**, *20*, 316–326. <https://doi.org/10.1154/1.2135315>.
- (73) Nečas, D.; Klapetek, P. Gwyddion: An Open-Source Software for SPM Data Analysis. *Open Phys.* **2012**, *10*, 181–188. <https://doi.org/10.2478/s11534-011-0096-2>.
- (74) Shannon, R. D.; Prewitt, C. T. Effective Ionic Radii in Oxides and Fluorides. *Acta Crystallogr. Sect. B Struct. Crystallogr. Cryst. Chem.* **1969**, *25*, 925–946. <https://doi.org/10.1107/S0567740869003220>.
- (75) Krasilin, A. A.; Suprun, A. M.; Nevedomsky, V. N.; Gusarov, V. V. Formation of Conical $(\text{Mg,Ni})_3\text{Si}_2\text{O}_5(\text{OH})_4$ Nanoscrolls. *Dokl. Phys. Chem.* **2015**, *460*, 42–44. <https://doi.org/10.1134/S0012501615020049>.
- (76) Krasilin, A. A.; Gusarov, V. V. Redistribution of Mg and Ni Cations in Crystal Lattice of Conical Nanotube with Chrysotile

- Structure. *Nanosyst. Physics, Chem. Math.* **2017**, *8*, 620–627. <https://doi.org/10.17586/2220-8054-2017-8-5-620-627>.
- (77) Demichelis, R.; De La Pierre, M.; Mookherjee, M.; Zicovich-Wilson, C. M.; Orlando, R. Serpentine Polymorphism: A Quantitative Insight from First-Principles Calculations. *CrystEngComm* **2016**, *18*, 4412–4419. <https://doi.org/10.1039/C6CE00190D>.
- (78) Hazen, R. M. Effects of Temperature and Pressure on the Crystal Structure of Forsterite. *Am. Mineral.* **1976**, *61*, 1280–1293.
- (79) Kanzaki, M.; Xue, X. Protoenstatite in MgSiO₃ Samples Prepared by Conventional Solid State Reaction. *J. Mineral. Petrol. Sci.* **2017**, *112*, 359–364. <https://doi.org/10.2465/jmps.170616>.
- (80) Thomassen, L. An X-Ray Investigation of the System Cr₂O₃-NiO 1. *J. Am. Chem. Soc.* **1940**, *62*, 1134–1136. <https://doi.org/10.1021/ja01862a037>.
- (81) L'vov, B. V.; Galwey, A. K. The Mechanism and Kinetics of NiO Reduction by Hydrogen. *J. Therm. Anal. Calorim.* **2012**, *110*, 601–610. <https://doi.org/10.1007/s10973-011-2000-0>.
- (82) Downs, R. T.; Palmer, D. C. The Pressure Behavior of α Cristobalite. *Am. Mineral.* **1994**, *79*, 9–14.
- (83) Post, J. E.; Bish, D. L.; Heaney, P. J. Synchrotron Powder X-Ray Diffraction Study of the Structure and Dehydration Behavior of Sepiolite. *Am. Mineral.* **2007**, *92*, 91–97. <https://doi.org/10.2138/am.2007.2134>.
- (84) Suh, I.-K.; Ohta, H.; Waseda, Y. High-Temperature Thermal Expansion of Six Metallic Elements Measured by Dilatation Method and X-Ray Diffraction. *J. Mater. Sci.* **1988**, *23*, 757–760. <https://doi.org/10.1007/BF01174717>.
- (85) Almjasheva, O. V.; Gusarov, V. V. Effect of ZrO₂ Nanocrystals on the Stabilization of the Amorphous State of Alumina and Silica in the ZrO₂-Al₂O₃ and ZrO₂-SiO₂ Systems. *Glas. Phys. Chem.* **2006**, *32*, 162–166. <https://doi.org/10.1134/S1087659606020064>.
- (86) Mokhov, V. M.; Popov, Y. V.; Nebykov, D. N. Hydrogenation of Alkenes over Nickel Nanoparticles under Atmospheric Pressure of Hydrogen. *Russ. J. Org. Chem.* **2016**, *52*, 319–323. <https://doi.org/10.1134/S1070428016030040>.
- (87) Konda, S. S. M.; Caratzoulas, S.; Vlachos, D. G. Computational Insights into the Role of Metal and Acid Sites in Bifunctional Metal/Zeolite Catalysts: A Case Study of Acetone Hydrogenation to 2-Propanol and Subsequent Dehydration to Propene. *ACS Catal.* **2016**, *6*, 123–133. <https://doi.org/10.1021/acscatal.5b01686>.
- (88) Witsuthammakul, A.; Sooknoi, T. Selective Hydrodeoxygenation of Bio-Oil Derived Products: Ketones to Olefins. *Catal. Sci. Technol.* **2015**, *5*, 3639–3648. <https://doi.org/10.1039/C5CY00367A>.

